

## Charge-exchange processes in titanium-doped sapphire crystals. I. Charge-exchange energies and titanium-bound excitons

Wing C. Wong and Donald S. McClure

*Department of Chemistry, Princeton University, Princeton, New Jersey 08544*

Sergei A. Basun

*A. F. Ioffe Physicotechnical Institute, Academy of Sciences of Russia, 194021, St. Petersburg, Russian Federation*

Milan R. Kokta

*Union Carbide, Chemicals and Plastics Company Inc., 750 South 32 Street, Washougal, Washington 98671*

(Received 19 September 1994)

The photoionization of  $Ti^{3+}$  in sapphire  $\alpha-Al_2O_3$  was studied by means of one-step and two-step photoconductivity measurements. An absorption band of  $Ti^{3+}$  at 2700 Å was shown to be due to a  $Ti^{3+}$  localized exciton. One-photon photoconductivity begins at the high-energy side of this band and thus the photoionization threshold can be located at  $4.71 \pm 0.07$  eV. The two-photon photoconductivity spectrum is nearly coincident with the excited state absorption and is shifted 0.6 eV to higher energy than the one-photon spectrum, due to the effect of the Jahn-Teller distortion of the  ${}^2E$  initial state. The origin of the transition due to valence band electron capture by  $Ti^{4+}$  is located at 4.17 eV. These electron and hole ionization energies are compared to values obtained by Born cycle calculations. Their sum is 0.5 eV less than the band gap of  $Al_2O_3$ .

### I. INTRODUCTION

Charge-exchange processes between a dopant and the host crystal include electron transfer from the dopant to the host (photoionization, PI, or donor transition) and the reverse (charge-transfer transition, CT, or acceptor transition). These two processes for  $Ti^{3+}$  and  $Ti^{4+}$  impurities in an  $Al_2O_3$  host crystal are correlated in this research. Although the charge-transfer band of  $Al_2O_3:Ti^{4+}$  and the photoionization of  $Al_2O_3:Ti^{3+}$  have been studied before, we found that a more detailed spectroscopic study of both processes was necessary to show how the two are related.

These two processes for the impurity  $Ti^{3+}$ ,  $Ti^{4+}$  in the host  $Al_2O_3$  are correlated in this research and the absolute position of the  $Ti^{3+}/Ti^{4+}$  dopant level within the band gap of the host crystal is determined. This is important since these nonlocalized electronic transitions produce charge carriers that are essential for the functioning of photon detectors but they are also the sources of excited-state absorption in solid-state tunable vibronic lasers.

Previously, Basun *et al.*<sup>1,2</sup> measured the photoconductivity of  $Ti^{3+}:Al_2O_3$ , but did not determine the exact threshold for photoionization. They used a two-step excitation; the first step excites the  ${}^2T_2 \rightarrow {}^2E$  transition of  $Ti^{3+}$  and the second step excites the  ${}^2E \rightarrow$  conduction band transition. We have carried out similar experiments but have used a tunable laser for the second step. The onset of the photocurrent is located and at the same time, we measured the excited state absorption. The results of this experiment are compared to the photocurrent threshold measured in a single step.

The onset of the charge-transfer process  $Ti^{4+} + e^-(VB) \rightarrow Ti^{3+}$  was estimated from the  $Ti^{4+}$  blue

emission and the corresponding blue luminescence excitation spectra. The luminescences of this material have been studied previously.<sup>3-6</sup> Further refinement in locating the charge-transfer threshold will be discussed in part II.<sup>7</sup> These donor and acceptor energy thresholds should be related to the band gap energy, and we discuss this relationship in the last section of this paper.

### II. EXPERIMENT

#### A. Sample preparation

One of the two titanium-doped sapphire crystals used in this work was given by Payne of the Lawrence Livermore National Laboratory (sample *A*). The other sample was given by the Union Carbide Corporation (sample *B*). The two crystals have different concentrations of  $Ti^{3+}$  and  $Ti^{4+}$  (see below). This allows comparisons to be made for the effect of capture and trapping centers on the photoconductivity and thermoluminescence [see part II (Ref. 7)]. The crystals from Union Carbide were grown by the Czochralski pulling technique in inert or reducing atmosphere.<sup>8</sup> Aluminum oxide containing the desired concentration of dopant  $Ti_2O_3$  was melted in an iridium crucible by means of radio frequency heating under an atmosphere of pure nitrogen or mixture of nitrogen with 1% by volume of hydrogen. Crystals were grown with orientation perpendicular to the  $\hat{c}$  axis. The pulling rates employed were 0.025 in. with rotation rate of 5 rpm. The growing method of the crystal from Lawrence Livermore is not known. Nevertheless, the much higher optical density in the UV region (due to  $Ti^{4+}$ ) suggests that more oxidizing conditions were used than for the other sample.

The crystals were cut into 1–2-mm-thick slices and fine polished on four sides. They were prepared such that

TABLE I. Optical properties of the Ti<sup>3+</sup>-doped sapphire crystals.

Sample	Concentrations of		<i>d-d</i> band ZPL energy (eV)	Jahn-Teller energy (eV)	Lifetime at		<sup>2</sup> T <sub>2</sub> → <sup>2</sup> E absorption band			
	Ti <sup>3+</sup> (10 <sup>18</sup> /cm <sup>3</sup> )	Ti <sup>4+</sup> (10 <sup>18</sup> /cm <sup>3</sup> )			300 K (μs)	10–20 K (μs)	Peak 1 (10 <sup>3</sup> cm <sup>-1</sup> )	FWHM (10 <sup>3</sup> cm <sup>-1</sup> )	Peak 2 (10 <sup>3</sup> cm <sup>-1</sup> )	FWHM (10 <sup>3</sup> cm <sup>-1</sup> )
<i>A</i>	21	2.9	2.01 <sup>a</sup>	0.381 <sup>a</sup>	3.0	3.8 <sup>b</sup>	18.2	1.60	20.4	3.19
<i>B</i>	5.9	0.073								

<sup>a</sup>Reference 13.<sup>b</sup>Reference 14.

the unique axis ( $\hat{c}$ ) is parallel to one of the long edges. The Ti<sup>3+</sup> and Ti<sup>4+</sup> concentrations were determined by methods to be discussed in later sections of this paper, but are listed in Table I.

### B. Optical measurements

Absorption spectra were taken in the range 200–800 nm using a Hewlett Packard 8450A Diode Array Spectrophotometer. Glan-air prisms were used to obtain the sigma-polarized ( $\perp\hat{c}$ ) and pi-polarized ( $\parallel\hat{c}$ ) spectra. Absorption below 200 nm was measured for sample *B* using a microwave discharge H<sub>2</sub> lamp and a helium-flushed ISA H-20 monochromator equipped with a Hamamatsu R1220 Cs-Te PMT.

The *d-d* visible emission was excited by the 532-nm second harmonic of a Quantel International 580-10 Nd:YAG laser. The spectra were taken using an ISA DH-10 double monochromator and a Hamamatsu R928 PMT. Time-resolved signals were averaged with a Nicolet 4094C digital oscilloscope. Ti<sup>4+</sup> CT luminescence excitation spectra were taken using a Perkin Elmer Model LS 50 luminescence spectrometer at room temperature RT.

The *d-d* luminescence excitation spectrum originating from the exciton band was taken from 10 to 300 K. The UV exciting light was obtained from a 2000-W xenon arc lamp through the H-20 monochromator (bandwidth = 4 nm). The signal was detected by a thermoelectrically cooled RCA C31034 GaAs photomultiplier tube through the DH-10 double monochromator.

### C. One-step photoconductivity

The experimental setup is similar to the one used by earlier workers.<sup>9</sup> The noise level was about 10<sup>-15</sup> A and the signal was typically 10<sup>-12</sup> to 10<sup>-14</sup> A. The highest photocurrent was stationary for minutes without any sign of polarization. A Glan polarizer was used for taking the polarized photoconductivity spectra. The signal was normalized into current per unit electric-field strength per incident photon. The photocurrent as a function of wavelength was measured twice at room temperature and then twice at liquid-nitrogen temperature (LNT). After this, the electric field was turned off and the crystal was subjected to 15 min to half an hour of UV irradiation (230 nm) at LNT. After the irradiation, the signal was taken again at LNT. The purpose of this procedure was to investigate the buildup of radiation produced defects.

### D. Two-step photoconductivity

The experimental setup was briefly mentioned in a previous paper.<sup>10</sup> Details are included here.

Two cylindrical SI-UV quartz lenses (focal length = 20 cm) were used to direct the two counter-propagating laser pulses sideways into the sample. In addition to two irises, one of the lenses was attached to an XYZ precision positioner to optimize the spatial overlapping of the light pulses. The pumping laser pulse was the 532-nm second-harmonic split from the Nd:YAG laser. The ionizing laser pulse was obtained from a Lambda Physik FL 3002 dye laser, which was pumped by the same Nd:YAG laser. The output from the dye laser was frequency doubled into the UV region by an Inrad Autotracker II Servotuning system from Interactive Radiation. A Glan-air polarizer was used to reject the fundamental light after frequency doubling. When the wavelength of the ionizing pulse was between 350 and 540 nm, a Moletron DL-II dye laser pumped by a Moletron UV 24 nitrogen laser (synchronized with the Nd:YAG laser) was used. This laser was also used in the experiment when the time delay between the pumping and ionizing pulse was varied (using a Stanford Research Systems DG535 four-channel digital delay/pulse generator).

The pulse-to-pulse fluctuations of the laser outputs were corrected by referencing the reflection intensities. The absolute intensities of the laser pulses were measured with a Scientech 361 power meter. The typical powers for the pumping and ionizing beams were about 10 mJ per pulse and 3 mJ per pulse, respectively (10-ns half-widths). The physical size of the ionizing pulse (~4 mm by 0.2 mm) was smaller than the pumping pulse (~9 mm by 0.5 mm).

The sample was kept between two electrodes inside a double-wall Dewar. The outside of the Dewar was shielded with grounded copper foil. To minimize current leakage and capacitance, electrical connection to and from the sample was made through two nickel wires that were glued into two clean supersil grade thin quartz tubes.

The electric field was applied perpendicular to the direction in which light propagated. Unlike the one-step photoconductivity, the signal decreased in the presence of the light pulses because of polarization. To solve this problem, a high voltage relay was used to alternate the polarity of the electric field to keep polarization from building up. The detector consisted of an electrometer grade monolithic operational amplifier AD549H from Analog

Devices. With the very low input bias current (75 fA) and input offset voltage (0.3 mV), it was used as a preamplifier. The amplifier was a low-noise precision PMI OP27. The overall response of the detector was a sensitivity of 0.1V/nA and a time constant of about 50  $\mu$ s. The detector was protected by two Zener diodes which clamped the input voltage to  $\pm 3.5$  V.

The output from the detector was fed into two Stanford Research Systems SR250 gated integrator boxcars. One of the boxcars had its gate fixed at the peak of the signal while the other was fixed 0.2 ms after the signal. The difference between these was used in order to minimize the low-frequency noise.

Photoconductivity was measured at both 300 and 77 K. Photocurrent as a function of the applied voltage, pumping beam, and ionizing beam intensities were also measured.

### E. Excited-state absorption

For the region near to the photoionization threshold, the excited-state absorption (ESA) was measured in parallel to the two-step photoconductivity. The ESA was measured as transmittance in the presence and absence of the pumping pulse. Then the ESA cross section at a particular wavelength was calculated from the intensity, the dimension of the pumping beam, and the  $\text{Ti}^{3+}$  ground-state absorption cross section. (The pumping power employed here is below the reported saturation fluence.<sup>11</sup>)

In another experiment, the ESA measurement was extended into the UV region (down to 240 nm) with 532-nm laser pulse for pumping and the xenon lamp as the probing source. The lamp output was tightly focused to ensure that only the pumped volume was probed.

## III. RESULTS AND DISCUSSION

### A. Optical absorption

The room-temperature absorption spectra for the two samples are shown in Fig. 1. The visible absorption consists of two bands, which are due to the Jahn-Teller split  ${}^2T_2 \rightarrow {}^2E$  transition of the  $\text{Ti}^{3+}$ .<sup>12</sup> The Gaussian-fitted half-widths and peak positions are shown in Table I. The results agree well with those reported in the literature.<sup>13,14</sup> The other optical properties are also included in Table I. According to the 490-nm absorption cross section ( $9.3 \pm 1.0 \times 10^{-20}$  cm<sup>2</sup>) found from magnetic and optical measurements,<sup>15</sup> the  $\text{Ti}^{3+}$  concentrations are 0.044 mol % ( $2.1 \times 10^{19}$  cm<sup>-3</sup>) in sample *A* and 0.013 mol % ( $5.9 \times 10^{18}$  cm<sup>-3</sup>) in sample *B*.

If the UV absorption were due to  $\text{Ti}^{3+}$  alone, then the ratio of the UV absorption to the visible absorption should be constant for different samples as both are directly proportional to  $\text{Ti}^{3+}$  concentration. Using a thinner slice of sample *A*, the normalized  $\sigma$  polarized spectra of the two samples are plotted together in Fig. 2. It can be seen that while the *d-d* band in the visible region has a ratio close to three, above 41 000 cm<sup>-1</sup>, sample *B* has a linear absorption coefficient that is about 35 times less than for sample *A*. It has been mentioned in the previous section that sample *B* was grown in a reducing atmo-

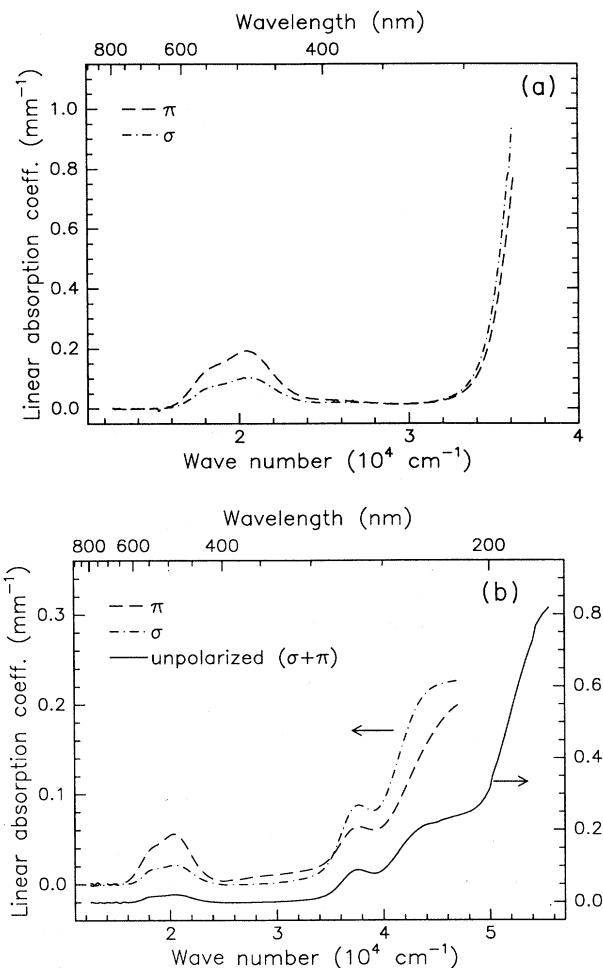


FIG. 1. 300-K polarized absorption spectra for the two  $\text{Ti}:\text{Al}_2\text{O}_3$  crystals. The absorbance  $[\ln(I_0/I)]$  is normalized into per unit thickness. (a) sample *A*. (b) sample *B*, showing the UV absorption to 55 000 cm<sup>-1</sup>.

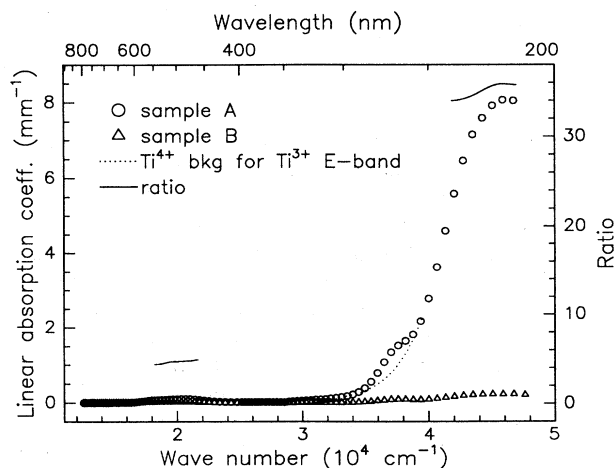


FIG. 2. *d-d* band-normalized  $\text{Ti}^{3+}$   $\sigma$ -polarized absorption spectra for the two differently grown  $\text{Ti}:\text{Al}_2\text{O}_3$  crystals at 300 K.

sphere and therefore should have a lower concentration of  $\text{Ti}^{4+}$ . The strong absorption in sample *A* is therefore due to  $\text{Ti}^{4+}$ , which has a  $d^0$  closed-shell electronic configuration. Its absorption is the result of a strongly allowed charge-transfer process. This is consistent with the previous results based on annealing.<sup>3-6</sup> Further support for this assignment can be found from the magnitude of photoconductivity below and trapping results in part II.<sup>7</sup> As shown in Fig. 1(b), other than the 270-nm band (which originates from  $\text{Ti}^{3+}$ , see Sec. III B below), there are two broad absorption bands at 220 and 180 nm. These are tentatively assigned to be the  $\text{O}^{2-} 2p$  to the  $\text{Ti}^{4+} 3d(t_2)$  and  $3d(e)$  CT transitions, respectively.

### B. Assignment of impurity-bound exciton

In addition to the strong UV absorption just associated with  $\text{Ti}^{4+}$ , there is a weaker band we call band *E* beginning at about 290 nm and peaking at 270 nm. Figure 1(b) shows this band at 300 K in relation to the visible *d-d* band for the more reduced sample *B*. Tippins assigned it to the  $\text{Fe}^{3+}$  charge-transfer band.<sup>16</sup> However, a survey of published spectra of  $\text{Ti}:\text{Al}_2\text{O}_3$  in the literature<sup>17-20</sup> shows that for different samples, the ratio of this band to the *d-d* band is nearly the same as for our sample for the same crystal orientation. For unpolarized light propagating along the  $\hat{c}$  axis, only the  $\sigma$  spectrum is seen, and the ratio  $I_E^\sigma/I_{d-d}^\sigma=2$ . In the  $\pi$  spectrum,  $I_E^\pi/I_{d-d}^\pi=0.6$ . Thus, it seems that band *E* is associated with  $\text{Ti}^{3+}$ . Based on EPR and Zeeman measurements, the lowest Kramers doublet of the electronic ground state  ${}^2T_2$  of  $\text{Ti}^{3+}$  in  $\text{Al}_2\text{O}_3$  ( $C_3$  site symmetry) belongs to the  $E_{3/2}$  representation.<sup>21,22</sup> The other two doublets  ${}^1E_{1/2}$  and  ${}^2E_{1/2}$  are 37.8 and 107  $\text{cm}^{-1}$  higher than the lowest  $E_{3/2}$ . At 300 K all three components of the ground multiplet are nearly equally populated. At 10 K, where only the lowest  $E_{3/2}$  component is populated, the absorption polarization ratio was found to be only slightly higher. Therefore it appears that the electric dipole transition strength is derived mainly from the  $E_{3/2}$  component. A transition  $E_{3/2} \rightarrow E_{1/2}$  is allowed in  $\sigma$  polarization. The *E* band has  $I_E^\sigma/I_E^\pi=3$ , which is partially in support of an assignment of  $E_{1/2}$  for the upper state. A state having  $E_{1/2}$  symmetry can arise from an *s*-like wave function coupled to the electron spin. Such an assignment was suggested by Reisfeld, Eyal, and Jorgensen.<sup>23</sup> However, it does not seem likely that the upper state wave function resembles a  $\text{Ti}^{3+}4s$  state since that state lies at 10 eV in the free ion,<sup>24</sup> and it has been shown that the  $d \rightarrow s$  transitions for ions in crystals are near to their free ion values at least for divalent transition metal ions.<sup>25</sup> It seems more likely that this *s*-like state is orthogonal to the  $4s$  Ti orbital and would be better described as a molecular orbital on the nearest-neighbor  $3s$  orbitals of the  $\text{Al}^{3+}$  ions. Such a description would help to explain why the intensity of the *E* band is not very different from that of the *d-d* band since the overlap of the Ti  $3d$  with the Al  $3s$  is small (the shortest Al-Al distance is 2.63 Å).

Further support for an assignment to a bound excited state of  $\text{Ti}^{3+}$  is that the photoconductivity does not begin until 260 nm, which is at higher energy than the peak of

band *E*. Band *E* is thus considered to be due to a localized exciton level. Moreover, this absorption band is absent from the spectrum of  $\text{Ti}^{4+}, \text{Mg}^{2+}:\text{Al}_2\text{O}_3$  (sample *C*) and hence it is not related to  $\text{Ti}^{4+}$ .

It was found that exciting the *E* band at low temperature gives rise to the *d-d* red emission. Its intensity is quenched strongly above 120 K. If the *E* band is indeed a  $\text{Ti}^{3+}$  exciton, then when it is excited at temperatures below that at which thermal ionization is rapid, it should decay into the  $\text{Ti}^{3+}$  manifold of levels, eventually giving the characteristic red luminescence of  $\text{Ti}^{3+}$ . The temperature dependence of the red emission intensity when excited at 270 nm is shown in Fig. 3. A kinetics model which fits the data is shown in the inset of Fig. 3. *p* is the population rate. *q* is the quantum yield of the *d-d* emission from the  ${}^2E$  level, which is constant below room temperature.<sup>26</sup> *p* can be assumed to be temperature independent as our absorption measurement indicates that the optical density of the 270-nm band stays almost the same from 300 K down to 4 K.  $k_1$  is the rate of thermal ionization.  $k_2$  is the nonradiative tunneling rate from the exciton to the  ${}^2E$  level.  $k_3$  is the thermally activated nonradiative decay from the exciton to the  ${}^2T_2$  level. More specifically,

$$k_1(T) = k_1(0)e^{-E_1/kT}, \quad (1)$$

$$k_2(T) = k_2(0), \quad (2)$$

$$k_3(T) = k_3(0)e^{-E_3/kT}. \quad (3)$$

Hence, the intensity of the red emission is

$$I_{\text{red}}(T) = \frac{k_2(T)}{\sum_{i=1}^3 k_i(T)} pq. \quad (4)$$

The fitting gives a thermal ionization rate constant,  $k_1(0) = 1.8 \times 10^5 \text{ s}^{-1}$  and an activation barrier,  $E_1 = 13 \text{ cm}^{-1}$ . The tunneling rate  $k_2(0)$  is about  $4.1 \times 10^4 \text{ s}^{-1}$ .  $k_3(0) = 1.3 \times 10^8 \text{ s}^{-1}$  and  $E_3 = 660 \text{ cm}^{-1}$ . This of course is a five-parameter fit to 11 data points, and may not be physically significant. The present results are significant

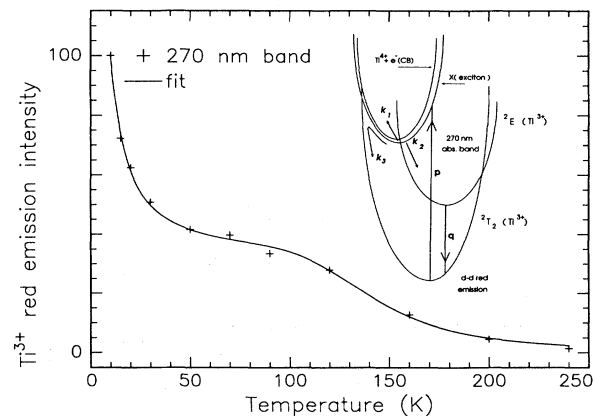


FIG. 3. Exciton band excitation efficiency (in arbitrary units) of the  $\text{Ti}^{3+} {}^2E \rightarrow {}^2T_2$  luminescence as a function of temperature from 10 to 250 K.

however in providing an example of an impurity ion in the act of ionizing. Further study of this exciton could reveal more details of the ionization process.

We also find similar titanium-bound exciton bands in other titanium-doped aluminate crystals (YAlO<sub>3</sub>, yttrium aluminum perovskite and LaMgAl<sub>11</sub>O<sub>19</sub>, lanthanum magnesium aluminum hexaaluminate).<sup>27</sup>

### C. One-step photoconductivity

The photoconductivity spectra are shown in Figs. 4 and 5. Only unpolarized light ( $\hat{k} \parallel \hat{\epsilon}$ ) and hence the  $\sigma$ -polarized spectrum was measured for sample *A* since the signal was weak. Figures 4(b) and 5(b) show the changes in the photocurrent after UV irradiation at 77 K. It can be seen that UV irradiation appreciably increased the photocurrent above 250 nm for sample *B* but it had virtually no effect on sample *A*. The photocurrent threshold

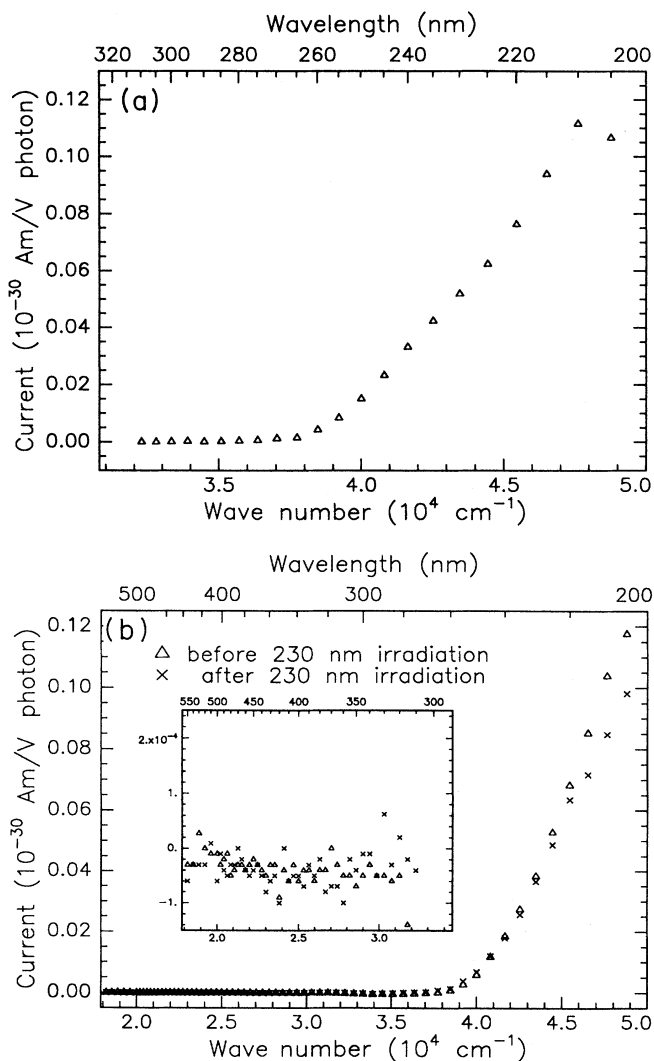


FIG. 4. (a) One-step  $\sigma$ -polarized photoconductivity spectrum for sample *A* at 300 K. (b) One-step  $\sigma$ -polarized photoconductivity spectra for sample *A* at 77 K (before and after 230-nm irradiation).

for sample *B* extends to about 500 nm even before irradiation while it is at about 260 nm for sample *A*. This long-wavelength photocurrent component can be erased either by warming the irradiated sample to 260 K or optically with 350-nm light at 77 K. Here, we relate the long-wavelength photocurrent component to the filling of electron traps upon irradiation at 230 nm. Detrapping can be achieved either thermally or optically. The mobility of holes is known to be much smaller than of electrons in pure sapphire.<sup>28</sup> This is consistent with the effective masses found from the calculated band structure.<sup>29</sup> Because of this, the current signal appearing in photoconductivity is mostly due to the electrons from Ti<sup>3+</sup> photoionization, as was verified by the thermoluminescence results to be given in part II.<sup>7</sup> Incidentally, the phenomenon of thermal erasure was observed before but no explanation was offered.<sup>19</sup> Because of the formation of these photochemical products, the photoconduction

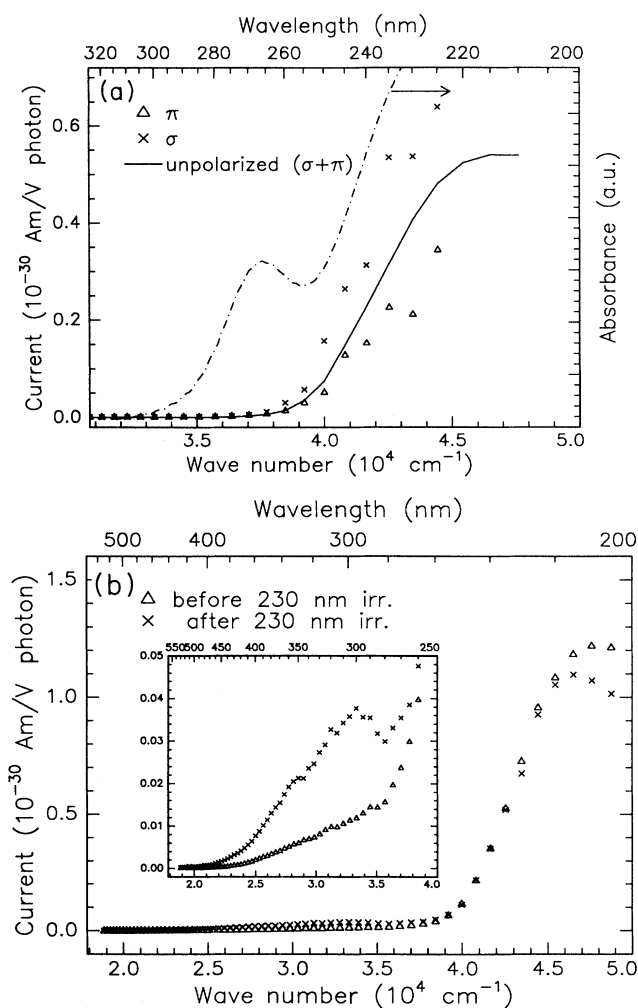


FIG. 5. (a) One-step photoconductivity and absorption spectra for sample *B* at 300 K. The photoionization threshold is determined by the rising edge of the current and the falling high-energy edge of the exciton absorption band. (b) One-step unpolarized photoconductivity spectra for sample *B* at 77 K (before and after 230-nm irradiation).

threshold may not be equal to the photoionization threshold for  $\text{Ti}^{3+}$ . Sample *A* did not exhibit this photochemical behavior perhaps because of the presence of abundant deep trapping centers, due to the higher  $\text{Ti}^{4+}$  concentration. Note that the  $\sigma$ -polarized photoconductivity spectrum of sample *B* [Fig. 5(a)] is stronger than the  $\pi$ -polarized spectrum. It is the same polarization ratio as band *E*, which we identified as the exciton band.

As shown in Fig. 2, the concentration of  $\text{Ti}^{4+}$  in sample *A* is about 35 times higher than in sample *B*. Based on the recently reported absorption cross section of  $\text{Ti}^{4+}:\text{Al}_2\text{O}_3$ ,<sup>30</sup> it follows that 1 and 10% of the Ti exists as  $\text{Ti}^{4+}$  in sample *B* and sample *A*, respectively.  $\text{Ti}^{4+}$  has two effects on the photocurrent: it reduces the light intensity, and acting as a deep trap it reduces the electron path length. Thus we can write for the value of the photocurrent (photopolarization)

$$P(\lambda) = I_0 F_1 (1 - e^{-(\alpha_1 N_1 + \alpha_2 N_2)x}) e z \\ = I_0 F_1 (1 - e^{-\rho}) e z ,$$

where

$$F_1 = \frac{\alpha_1 N_1}{\alpha_1 N_1 + \alpha_2 N_2} = \frac{\alpha_1 N_1 x}{\rho(\lambda)} ,$$

and is the fraction of the light absorbed by  $\text{Ti}^{3+}$  (species 1) in a sample of thickness  $x$ . The total optical density is  $\rho(\lambda)$  and the electron path length is  $z$ . In sample *B*,  $\rho$  is small and  $\text{Ti}^{4+}$  has little effect on the light distribution in the sample. In sample *A*, most of the light near the absorption peak at  $47\,000\text{ cm}^{-1}$  is absorbed in the first 0.1 mm, thus reducing the number of  $\text{Ti}^{3+}$  able to participate in the photoionization and overcoming the effect of the higher  $\text{Ti}^{3+}$  concentration in this sample.

At about  $47\,000\text{ cm}^{-1}$  near the first  $\text{Ti}^{4+}$  absorption peak [Fig. 1(b)], the photocurrent ratio is  $P_A/B = 1/6$ . The light distribution can account for a ratio of 1/2 and the remainder must be due to the shorter trapping distance in sample *A*.

The photocurrent spectra for the two samples are similar but not identical. The  $\text{Ti}^{4+}$  can affect the spectral shape of sample *A*, especially at the higher energies, but the precision of the data may not be high enough to justify drawing any special conclusions as to the small difference between the two samples.

The magnitudes of the photocurrent at 300 and 77 K are nearly the same (Fig 4 for sample *A* and Fig. 5 for sample *B*). This result means that the ionization is rapid and is not competing with a nonradiative return to the ground state. Near the threshold, however, the photocurrent is reduced measurably at 77 K compared to 300 K.

The photoionization threshold is determined by the rising edge of the photoconductivity spectrum and the falling high-energy edge of the exciton band [Fig. 5(a)]. Its value is thus bracketed by these two spectroscopic indicators, and appears to be  $38\,000 \pm 500\text{ cm}^{-1}$ , 4.71 eV. The presence of the exciton band makes it possible to eliminate most of the error in the threshold value due to the photoionization of trapped electrons. This value is to be compared with the 4.25-eV ionization limit for  $\text{Ti}^{3+}$

found previously from a high-temperature conductivity experiment.<sup>31</sup>

#### D. Two-step photoconductivity

In two-step photoconductivity, the dopant of interest is selectively excited and then a second photon is used to ionize it from the excited state. The delay between the two pulses can be varied to verify the identity of the ionizing species. In addition, two-step photoconductivity is particularly helpful when the spectral region where photoionization occurs is highly absorbing in the ground state. In some cases, the high optical density will lead to the signal being dominated by the property of the sample surface or carrier-carrier interaction.<sup>32,33</sup> In two-step condition, the excited species can be generated more uniformly inside the sample, making the study of bulk properties possible. Also, two-step photoconductivity can be used to access the high-energy region when conventional light sources become too weak to be used.

The photocurrent versus time delay between the pump pulse and ionize pulse for sample *B* is shown in Fig. 6. The  ${}^2E \rightarrow {}^2T_2$  emission decay is also plotted in the same figure. It can be seen that the electrical signal decreased exponentially with a rate that is close to the 300-K lifetime of the  $\text{Ti}^{3+}$  excited state,<sup>2</sup> proving that the signal originated from the excited  $\text{Ti}^{3+}$ .

Furthermore, the effect of light intensity on the photocurrent and ESA was measured to confirm the ionization mechanism. It was found that the signal was linearly dependent on the intensities of both the pump and the ionizing laser pulses.

The 300-K two-step photoconductivity spectrum for sample *B* is shown in Fig. 7. the 77-K data are similar and not shown. As in the case of one-step photoconductivity, the signal obtained from sample *A* gave the same threshold and trend but a photocurrent smaller by a factor of about 100. This ratio is inconsistent with the one-step photocurrent ratio and is not understood. While the larger amount of  $\text{Ti}^{4+}$  present in the sample will reduce the average range of the free electron and hence the

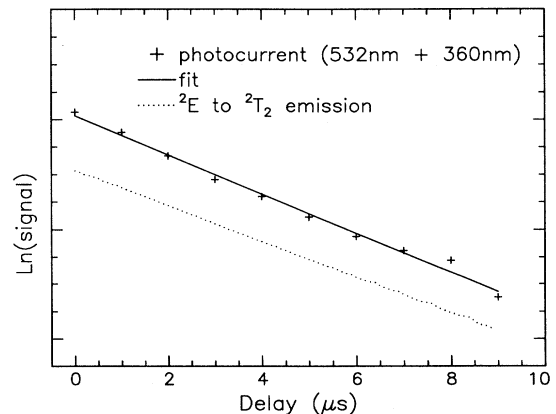


FIG. 6. Photocurrent vs delay between the two laser pulses (532 and 360 nm) for sample *B* at 300 K. Also shown is the emission decay excited by 532 nm.

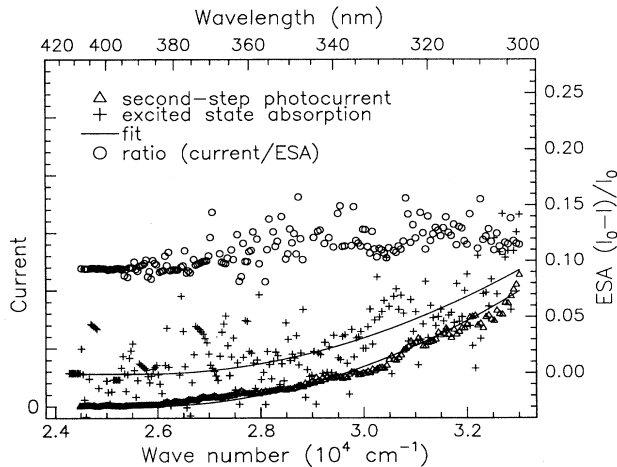


FIG. 7. Second-step photocurrent and ESA for sample *B* at 300 K. Ratio shows the photocurrent per absorbed photon. The abscissa is the experimental energy scale.

current, the excited-state absorption should not be affected. This is in fact the case since the  $\text{Ti}^{3+}$  ESA cross sections are found to be the same [ $10^{-18} \text{ cm}^2$  at 305 nm ( $\sigma$ )] for both samples. The second-step threshold was located at 3.19 eV by nonlinear least-squares fitting of the signal with a truncated second degree polynomial (Table II). Due to the weak absorption, the ESA signal was rather noisy. To allow the trend in the ESA to be seen in a clearer manner, a fitted line was drawn in Fig. 7. Despite the selectivity, the photoionization threshold cannot be located precisely from the two-step signal because of the small Franck-Condon factor at the threshold (Fig. 9 inset).

#### E. Excited-state absorption

The ESA measured in parallel to the two-step photoconductivity was found to begin and increase with the photocurrent signal (Fig. 7). Note that the noisy but noticeably increasing ratio of photocurrent to ESA is a result of the increasing ionization quantum yield as the photon energy increases. The ESA measurement extended to 250 nm is shown in Fig. 8 where the xenon lamp background was used for the second step. The absorption cross section increased with the energy of the probing photon monotonically. This is consistent with a previous result reported (to 280 nm).<sup>34</sup>

#### F. Comparison between one-step and two-step photoconductivities

In both the one-step and two-step photoconductivity spectra, a steady rise was found. This is due to a combination of the increasing ionization efficiency, density of states in the conduction band,<sup>35,36</sup> and the Franck-Condon factor.

It is important to realize that the information which can be obtained from one-step and two-step photoconductivities is not all the same. This is illustrated by the simplified  $e_g$  vibrational mode configuration diagram of a  $\text{Ti}^{3+}$  ion in an octahedral site of the host lattice (inset of Fig. 9). The intralelectronic vibrational relaxation from the  $|^2E\rangle|n\rangle$  state to the  $|^2E\rangle|0\rangle$  state was found to be about 3.5 ps.<sup>37</sup> The laser pulses used in this study have a FWHM of 10 ns. Therefore, the excited-state ionization from the  $|^2E\rangle|0\rangle$  state was measured. One might expect that the photoionization threshold from the one-step photoconductivity should be the same as the sum of the second-step photoconductivity threshold and the  $^2T_2 \leftrightarrow ^2E$  zero-phonon energy.

However, if a comparison is to be made between the photocurrent signal in the region above the threshold energy, it can be seen that the signal is shifted by an amount determined by the displacement of the  $\text{Ti}^{3+}$   $^2E$  excited state adiabatic potential curve relative to that of the  $\text{Ti}^{3+}$   $^2T_2$  ground-state potential curve, both projected onto the  $\text{Ti}^{4+}$   $^1A_1$  potential curve as shown in the inset of Fig. 9. The Jahn-Teller splitting in the  $\text{Ti}^{3+}$   $^2E$  state is considered to cause the largest displacement. As a result, the Jahn-Teller active  $e_g$  normal mode will account for most of the shift in the photocurrent spectra. The displacements in the  $a_g$  and  $e_g$  vibrational modes of  $\text{Ti}^{3+}$  have already been estimated to be 0.0442 and 0.409 Å, respectively.<sup>38</sup> The actual value of this shift in energy depends on the force constant of the  $e_g$  mode in the  $(\text{Ti}^{4+}-\text{O}_6^{2-})$  moiety. This information can be obtained from Raman-scattering studies. Because of the higher Coulombic potential, a rough approximation will be to use  $\frac{4}{3}$  of the  $e_g$  mode force constant in  $\text{Ti}^{3+}$  for  $\text{Ti}^{4+}$ . Then the energy shift will be  $\frac{4}{3}$  of the Jahn-Teller energy in the  $^2E$  state of  $\text{Ti}^{3+}$ . This calculation results in a shift of  $4100 \text{ cm}^{-1}$ .

In Fig. 9, the one-step and two-step photocurrent spectra are plotted together. The ZPL (zero phonon line) energy was added to the two-step signals. The vertical scales were adjusted until the curves have almost the same rising slope. Only 300-K data were used because as mentioned, the one-step 77-K data was affected considerably by the trapped species in the region of interest. The

TABLE II. Sums of PI and CT thresholds as compared with the  $E_g$  of the oxide crystals.

One-step photoionization threshold (eV)	$\text{Ti}^{4+}$ charge-transfer threshold (eV)	Second-step photoionization threshold (eV)	Sum of PI and CT thresholds (eV)	Optical band gap energy $E_g$ (eV)
4.71	4.17	3.19	8.88	9.4 <sup>a</sup>

<sup>a</sup>Reference 48.

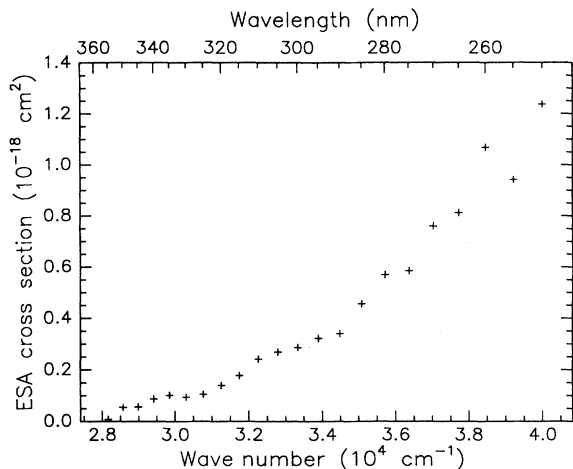


FIG. 8. ESA for sample *B* at 300 K extended to the UV region. The abscissa is the experimental energy scale.

shift in the energy coordinate is about  $5000 \text{ cm}^{-1}$ . This is not very different from the predicted value of  $4100 \text{ cm}^{-1}$  based on the assumptions made above.

### G. Charge-transfer transition

The  $\text{Ti}^{4+}$  CT band has a high oscillator strength, yet the relatively large change in the adiabatic potential curve between the ground and excited states gives rise to a very large Stokes shift so that the zero-phonon line is not observable. Blue luminescence from titanium-doped  $\text{Al}_2\text{O}_3$  excited by UV light has been reported by different workers.<sup>3-6,39</sup> They attributed the emission to the radiative relaxation from the  $\text{Ti}^{4+}$  charge-transfer transition. The emission spectrum excited at 240 nm and the fluorescence excitation spectrum were recorded and shown in Fig. 10. Unlike the absorption spectrum, the blue emission excitation spectrum showed a peak at 230 nm.

The electronic origin of the charge-transfer band as the mean of the 420-nm emission peak and the 230-nm exci-

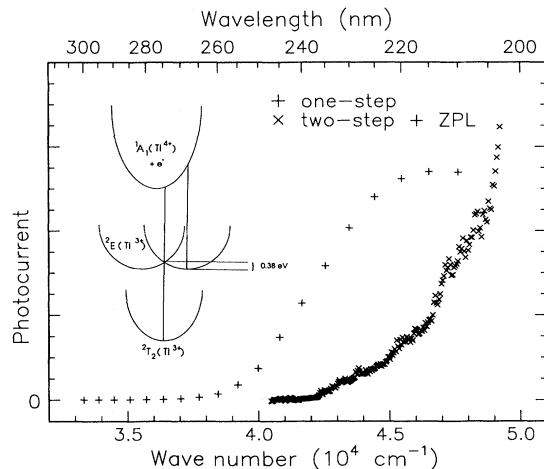


FIG. 9. Comparison between one and two-step photocurrent spectra for sample *B* at 300 K. For the two-step photocurrent,  $16\,200 \text{ cm}^{-1}$  is added to the abscissa.

tation peak is 4.17 eV (Table II). This value is very close to the estimation of the lowest charge-transfer band using Jorgensen's optical electronegativity:<sup>40,41</sup>

$$V_{\text{CT}} = 30\,000[\lambda_{\text{opt}}(\text{O}^{2-}) - \chi_{\text{opt}}(\text{Ti}^{4+})] \text{ cm}^{-1},$$

With  $\chi_{\text{opt}}(\text{O}^{2-}) = 3.2$  and  $\chi_{\text{opt}}(\text{Ti}_{\text{Octahedral}}^{4+}) = 2.05$ ,<sup>42</sup> the charge-transfer band is predicted to be at 4.3 eV.

A more detailed treatment of the charge-transfer states will be given in the next paper,<sup>7</sup> where the emitting state will be assigned as a triplet. This new assignment causes a slight change in the zero-phonon energy of the charge-transfer state.

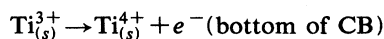
### H. Born cycle model for the localized levels of Ti in the band gap of the host

Photoionization and charge-transfer energy thresholds for a dopant can be calculated based on thermodynamic cycles involving the following steps:

- (1)  $\text{Ti}^{3+}(\text{site}) \rightarrow \text{Ti}^{3+}(\text{vacuum}), E_1 = eV_3,$
- (2)  $\text{Ti}^{3+}(\text{vacuum}) \rightarrow \text{Ti}^{4+}(\text{vacuum}) + e^-(\text{vacuum}), E_2 = I_4(\text{Ti}),$
- (3)  $\text{Ti}^{4+}(\text{vacuum}) \rightarrow \text{Ti}^{4+}(\text{site}), E_3 = -eV_4,$
- (4)  $e^-(\text{vacuum}) \rightarrow e^-(\text{bottom of CB}), E_4 = -\chi,$

where  $e$  is the charge of electron;  $V_3$  and  $V_4$  are the total potential at the  $\text{Al}^{3+}$  crystal site for  $\text{Ti}^{3+}$  and  $\text{Ti}^{4+}$ , and  $\Delta V(\text{site}) = V_4 - V_3$ ;  $I_4(\text{Ti})$  is the fourth ionization potential of Ti (43.268 eV);<sup>43</sup>  $\chi$  is the electron affinity of the crystal.

The photoionization threshold is given by



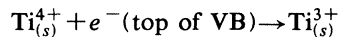
with energy

$$E_{\text{PI}} = I_4(\text{Ti}) - \Delta V(\text{site}) - \chi. \quad (5)$$

The corresponding processes and quantities for the charge-transfer transition are

- (1)  $\text{Ti}^{4+}(\text{site}) \rightarrow \text{Ti}^{4+}(\text{vacuum})$   $E_1 = eV_4$ ,
- (2)  $e^-(\text{top of VB}) \rightarrow e^-(\text{bottom of CB})$ ,  $E_2 = E_g$ ,
- (3)  $e^-(\text{bottom of CB}) \rightarrow e^-(\text{vacuum})$ ,  $E_3 = \chi$ ,
- (4)  $\text{Ti}^{4+}(\text{vacuum}) + e^-(\text{vacuum}) \rightarrow \text{Ti}^{3+}(\text{vacuum})$ ,  $E_4 = -I_4(\text{Ti})$ ,
- (5)  $\text{Ti}^{3+}(\text{vacuum}) \rightarrow \text{Ti}^{3+}(\text{site})$ ,  $E_5 = -eV_3$ ,

where  $E_g$  is the band gap energy of the host crystal. The charge-transfer threshold is given by



with energy

$$E_{\text{CT}} = E_g + \Delta V(\text{site}) - I_4(\text{Ti}) + \chi. \quad (6)$$

It is to be emphasized that the quantities in Eqs. (5) and (6) are for the relaxed thermodynamic states at 0 K (i.e., zero-phonon-line energies). A test of the thermodynamic model calculations is to compare the measured  $E_{\text{PI}}$  or  $E_{\text{CT}}$  with Eq. (5) or (6). Stoneham, Sangster, and Tasker<sup>44</sup> have modeled these comparisons for divalent transition metal ions in MgO where shell-model potentials and an energy minimization using the HADES program were used to find the energies analogous to our  $V_3$  and  $V_4$ . Instead of this excellent calculation we approximated  $V_4 - V_3 = \Delta V$  by the electrostatic potential at an  $\text{Al}^{3+}$  site (neglecting relaxation at the impurity site). This was calculated by the Madelung sum performed with the Ewald method. For the (12c) site in  $\text{Al}_2\text{O}_3$  the value was found to be  $-36.58$  eV.<sup>45</sup> The electron affinity of sapphire  $\chi$  was reported to be about 1 eV.<sup>46</sup> The band gap energy of  $\text{Al}_2\text{O}_3$  reported from different sources show values from 7 to 10.35 eV. The lower values must be due to the impurities in the sample. Although the quality of contemporary synthetic sapphire is good, erroneous assignments for  $E_g$  are still given. The optical  $E_g$  should be above 9 eV since the exciton absorption of pure sapphire

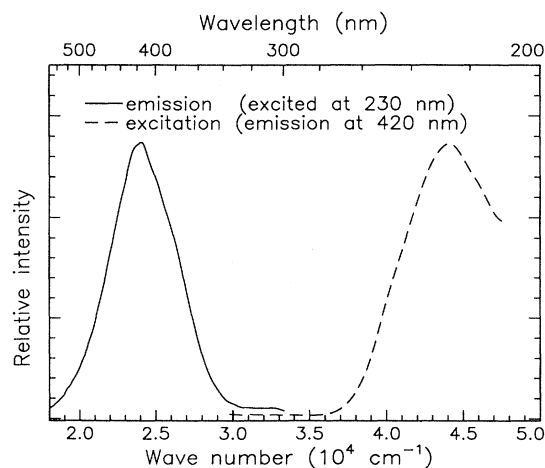


FIG. 10. Emission and excitation band of  $\text{Ti}^{4+}$  in sample *B* at 300 K.

peaks at 9 eV.<sup>47</sup> A more recent determination based on high-temperature electrical conductivity gives  $9.4 \pm 0.2$  eV as the thermal band gap at 0 K.<sup>48</sup> This energy coincides with the absorption minimum just above the exciton band, so we believe this is the correct value to use. (In Ref. 10, we incorrectly took  $E_g$  to be 8.5 eV.) When these values are used in Eqs. (5) and (6), the photoionization and charge-transfer thresholds are found to be 5.69 and 3.82 eV, respectively. These values are not very far from the experimental values (4.71 and 4.17 eV).

The sum of Eqs. (5) and (6) gives the deceptively simple result

$$E_g = E_{\text{PI}} + E_{\text{CT}}. \quad (7)$$

Figure 11 shows that the zero-phonon energies for photoionization and charge transfer add up to the band gap, provided the electron and hole are far from their sources.<sup>49</sup> In a spectroscopic transition the latter conditions are never fulfilled so that special corrections must be made to find thermodynamic energies from the spectral ones.

In the present case of  $\text{Ti}^{3+}$ ,  $\text{Ti}^{4+}$  in  $\text{Al}_2\text{O}_3$ , our measurements given in Table II show that the sum is  $9.4 - (4.71 + 4.17) = 0.5$  eV short of the band gap energy. We have made other such comparisons which show a similar level of agreement.<sup>10</sup>

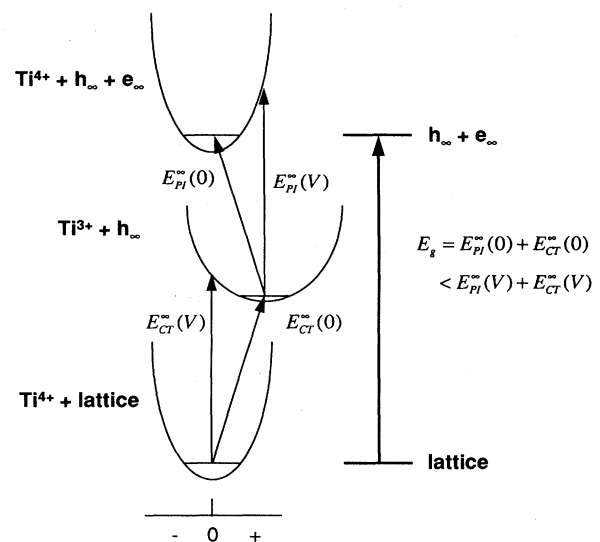


FIG. 11. Potential curves for  $\text{Ti}^{3+}$  photoionization and  $\text{Ti}^{4+}$  charge-transfer transition, showing zero-phonon transitions and vertical transitions.

## IV. CONCLUSIONS

Titanium exists in more than one charge state in sapphire. Together with the exciton band, the photoionization energy thresholds of  $Ti^{3+}$  were located from one-step photocurrent measurements. The uncertainty of using one-step photoconductivity alone to locate the threshold energy is illustrated. The identification of the exciton band, however, enables a good estimate of the threshold to be made. The selectivity of two-step photoconductivity is demonstrated. The shift in the photocurrent spectra in the two-step from the one-step signal is explained by the change in the equilibrium Ti-O distance in the configuration energy diagram. The charge-transfer transition energy threshold for  $Ti^{4+}$  was obtained through optical measurements. The calculated values of photoionization and charge-transfer thresholds using the local electrostatic potentials at the cation site were in reasonable agreement with the experimental values. Quantitatively, the sums of the two thresholds are found to give approximately the band gap energy of the host crystal.

This offers a convenient way for material characterization. Provided that the band gap energy of the material is known and the charge transfer can be observed optically, the photoionization threshold can be estimated. One reason that  $Ti^{3+}:Al_2O_3$  is a good vibronic laser material is that the second step photoconductivity threshold is greater than the  ${}^2E \rightarrow {}^2T_2$  zero-phonon energy as has been shown in detail in this paper.

## ACKNOWLEDGMENTS

We want to thank the Union Carbide Corporation and Stephen Payne of the Lawrence Livermore National Laboratory for providing us the crystals and Douglas Johnson of the Geology Department in Princeton University for preparing the crystal samples. The work was supported in part by the National Science Foundation under Grant No. EAR 89-17292 and by the Department of Chemistry. S.B. acknowledges with thanks a grant from the program Cooperation in Applied Science and Technology (CAST), administered by the National Research Council.

- <sup>1</sup>S. A. Basun, S. P. Feofilov, A. A. Kaplyanskii, B. K. Sevastyanov, M. Yu. Sharonov, and L. S. Starostina, *J. Lumin.* **53**, 28 (1992).
- <sup>2</sup>S. A. Basun, A. A. Kaplyanskii, V. K. Sevastyanov, L. S. Starostina, S. P. Feofilov, and A. A. Chernyshev, *Sov. Phys. Solid State* **32**, 1109 (1990).
- <sup>3</sup>T. S. Bessonova, M. P. Stanislavskii, and V. Ya. Khaimov-Malkov, *Opt. Spectrosc. (USSR)* **41**, 87 (1976).
- <sup>4</sup>R. C. Powell, G. E. Venikouas, L. Xi, J. K. Tyminski, and M. R. Kokta, *J. Chem. Phys.* **84**, 662 (1986).
- <sup>5</sup>R. C. Powell, in *Defect Properties and Processing of High-Techonology Nonmetallic Materials*, edited by Y. Chen, W. D. Kingery, and R. J. Stokes (Material Research Society, Pittsburgh, PA 1986), p. 395.
- <sup>6</sup>G. Blasse and J. W. M. Verweij, *Mater. Chem. Phys.* **26**, 131 (1990).
- <sup>7</sup>W. C. Wong *et al.*, following paper, *Phys. Rev. B* **51**, 5693 (1995).
- <sup>8</sup>M. R. Kokta, in *Laser and Nonlinear Optical Materials, SPIE Vol. 681*, edited by L. G. DeShazer (Bellingham, Washington, 1987), p. 50.
- <sup>9</sup>C. Pedrini, D. S. McClure, and C. H. Anderson, *J. Chem. Phys.* **70**, 4959 (1979).
- <sup>10</sup>W. C. Wong, D. S. McClure, and S. A. Basun, *J. Lumin.* **60&61**, 183 (1994).
- <sup>11</sup>L. G. DeShazer, J. M. Eggleston, and K. W. Kangas, *Opt. Lett.* **13**, 363 (1988).
- <sup>12</sup>D. S. McClure, *J. Chem. Phys.* **36**, 2757 (1962).
- <sup>13</sup>M. Yamaga, Y. Gao, F. Rasheed, K. P. O'Donnell, B. Henderson, and B. Cockayne, *Appl. Phys. B* **51**, 329 (1990).
- <sup>14</sup>P. Moulton, *J. Opt. Soc. Am. B* **3**, 125 (1986).
- <sup>15</sup>R. L. Aggarwal, A. Sanchez, R. E. Fahey, and A. J. Strauss, *Appl. Phys. Lett.* **48**, 1345 (1986).
- <sup>16</sup>H. H. Tippins, *Phys. Rev. B* **1**, 126 (1970).
- <sup>17</sup>K. Eigenmann, K. Kurtz, and Hs. H. Gunthard, *Helv. Phys. Acta* **45**, 452 (1972).
- <sup>18</sup>P. Albers, E. Stark, and G. Huber, *J. Opt. Soc. Am. B* **3**, 134 (1986).
- <sup>19</sup>H. Manaa, C. Pedrini, and R. Moncorge, in *OSA Proceedings on Advanced Solid-State Lasers, 1991*, edited by G. Dube and L. Chase (Optical Society of America, city, 1991), Vol. 10, p. 371.
- <sup>20</sup>T. Wegner and K. Petermann, *Appl. Phys. B* **49**, 275 (1989).
- <sup>21</sup>R. R. Joyce and P. L. Richards, *Phys. Rev.* **179**, 375 (1969).
- <sup>22</sup>B. F. Gaechter and J. P. Bentley, *Solid State Commun.* **14**, 361 (1974).
- <sup>23</sup>R. Reisfeld, M. Eyal, and C. K. Jorgensen, *Chimia* **41**, 117 (1987).
- <sup>24</sup>Atomic Energy Levels, Vol. 1, US Dept. of Commerce, National Bureau of Standard Circular 467 (1949).
- <sup>25</sup>D. B. Chase and D. S. McClure, *J. Chem. Phys.* **64**, 74 (1976).
- <sup>26</sup>P. Albers, E. Stark, and G. Huber, *J. Opt. Soc. Am. B* **3**, 134 (1986).
- <sup>27</sup>W. C. Wong, D. S. McClure, and S. A. Basun (unpublished).
- <sup>28</sup>R. C. Hughes, *Phys. Rev. B* **19**, 5318 (1979).
- <sup>29</sup>R. H. French, *J. Am. Ceram. Soc.* **73**, 477 (1990).
- <sup>30</sup>B. D. Evans, *J. Lumin.* **60&61**, 620 (1994).
- <sup>31</sup>S. K. Mohapatra and F. A. Kroger, *J. Am. Ceram. Soc.* **60**, 381 (1977).
- <sup>32</sup>E. Morikawa, Y. Isono, and M. Kotani, *J. Chem. Phys.* **78**, 2691 (1983).
- <sup>33</sup>Y. Isono, E. Morikawa, and M. Kotani, *Chem. Phys. Lett.* **125**, 344 (1986).
- <sup>34</sup>T. Danger, K. Petermann, and G. Huber, *Appl. Phys. A* **57**, 309 (1993).
- <sup>35</sup>J. Guo, D. E. Ellis, and D. J. Lam, *Phys. Rev. B* **45**, 3204 (1992).
- <sup>36</sup>Y. Xu and W. Y. Ching, *Phys. Rev. B* **43**, 4461 (1991).
- <sup>37</sup>S. K. Gayen, W. B. Wang, V. Petricevic, K. M. Yoo, and R. R. Alfano, *Appl. Phys. Lett.* **50**, 1494 (1987).
- <sup>38</sup>H. Eiles, E. Strauss, and W. M. Yen, *Phys. Rev. B* **45**, 9604 (1992).
- <sup>39</sup>B. Macalik, L. E. Bausa, J. Garcia-Sole, F. Jaque, J. E. Munoz Santieste, and I. Vergara, *Appl. Phys. A* **55**, 144 (1992).
- <sup>40</sup>C. K. Jorgensen, in *Progress In Inorganic Chemistry*, edited by S. J. Lippard (Wiley, New York, 1970), Vol. 12, p. 101.

- <sup>41</sup>A. Muller, E. Diemann, and C. K. Jorgensen, in *Structure and Bonding* (Springer-Verlag, New York, 1973), Vol. 14, p. 23.
- <sup>42</sup>A. B. P. Lever, *Inorganic Electronic Spectroscopy*, 2nd ed. (Elsevier, New York, 1986), p. 221.
- <sup>43</sup>J. Sugar and C. Corliss, *J. Phys. Chem. Ref. Data* **14**, Suppl. 2, 170 (1985).
- <sup>44</sup>A. M. Stoneham, M. J. L. Sangster, and P.W. Tasker, *Philos. Mag. B* **44**, 603 (1981).
- <sup>45</sup>S. Hafner and M. Raymond, *J. Chem. Phys.* **49**, 3570 (1968).
- <sup>46</sup>C. R. Viswanathan and R. Y. Loo, *Appl. Phys. Lett.* **21**, 370 (1972).
- <sup>47</sup>T. Tomiki, Y. Ganaha, T. Shikenbaru, T. Fudemma, M. Yuri, Y. Aiura, S. Sato, H. Fukutani, H. Kato, T. Miyahara, A. Yonesu, and J. Tamashiro, *J. Phys. Soc. Jpn.* **62**, 573 (1993); T. Tomiki, Y. Ganaha, T. Fudemma, T. Shikenbaru, Y. Aiura, M. Yuri, S. Sato, H. Fukutani, H. Kato, T. Miyahara, J. Tamashiro, and A. Yonesu, *ibid.* **62**, 1372 (1993).
- <sup>48</sup>F. G. Will, H. G. deLorenzi, and K. H. Janora, *J. Am. Ceram. Soc.* **75**, 2790 (1992).
- <sup>49</sup>D. S. McClure, W. C. Wong, and S. A. Basun (unpublished).